High-quality phase plates verify a 3D printing workflow that reduces fabrication time of self-manufactured DOEs

Koen Jurgens

Department of Imaging Physics, Delft University of Technology, Lorentzweg 1, 2628CJ Delft, The Netherlands.

Abstract

Diffractive optical elements (DOEs) are expensive devices that are integrated into optical set-ups to controllably engineer the shape and amplitude of light. A low-cost alternative is the self-manufacturing with 3D printing technology, but defects are regularly introduced due to limited printing resolution. The fabrication process becomes less challenging when the DOE dimensions are scaled up > 100 times by immersing a DOE in a solution that nearly matches its refractive index. However, this trick significantly increases the fabrication time as well. Here, we present two different phase plates, produced with a workflow that can be executed in one working day, whereby one phase plate did not lose any functionality or quality. The point spread function (PSF) with and without the phase plates was simulated and subsequently measured to assess the phase plate performance. In addition, the devices could be easily implemented in our microscope set-up, implying the extensive applicability of DOEs.

Layman's Summary

Traditional optical components (such as lenses and mirrors) in light microscopes are able to change the direction of the light beam that travels through a microscope, but they cannot manipulate the shape of the beam. Therefore, diffractive optical elements (DOEs) have been developed to do exactly that. Shaping, splitting or generating a specific pattern in the beam are some examples of unique outputs that can be created with DOEs. If only a few DOEs are ordered from a company, fabricating and delivering these devices are slow and pretty expensive. A cheap solution is using 3D printing technology, which has vastly evolved over the years to make the self-manufacturing of DOEs possible. However, defects in fine features of DOEs occur frequently, because the printing resolution of a 3D printer is only roughly 100 nm at best. The fabrication of phase plates is a striking example whereby the issue of limited resolution is encountered. Phase plates are DOEs that create phase delays in the light beam through their pattern and thickness. They are usually made of a high refractive index material. The refractive index is an indication of how much the speed of light is reduced with respect to vacuum when entering a certain medium. The height for phase plates should normally be around 1 µm, so it is only 10x larger than the printing resolution. The fine features will therefore be printed too coarse, resulting in an ineffective phase plate. Recently, one research group demonstrated a method to simplify the phase plate self-manufacturing. The researchers showed that the phase plate height can be scaled up more than 100 times by immersing the phase plates in a liquid with a refractive index similar to the material of the phase plate. The phase of light is changed more slowly, so the light must travel through more material. However, it is important that the refractive indices do not have the same value, because this negates the effect. The method worked really well, but the fabrication is a labour-intensive job that takes up one whole working week.

We have figured out a workflow consisting of three steps to significantly reduce the fabrication time back to one working day. First, a very practical 3D model was designed for two different kinds of phase plates. The model included all features of the phase plates, and an easy way to customize the dimensions of the phase plates. Next, these phase plates were realized with our 3D printer, which took approximately five hours per phase plate. The last step was the immersion process, which can be done very quickly owing to a certain property of the immersion substance we used. The substance is supplied as a liquid, but it becomes a solid material when it is exposed to high intensities of UV light. Thus, we pour the immersion liquid over the phase plate, and simply place the devices under a nail dryer for 5 minutes to solidify the substance. This makes the phase plates easy to handle, which is a great advantage when we needed to integrate them into our microscope set-up to examine their quality. We first simulated and then imaged the induced effects by the phase plates on a very small spherical object. In the simulation, the dimensions of the phase plates are perfect, which is near-impossible to replicate in real life. Based on the acquired experimental data, we concluded that the one 3D printed, immersed phase plate did not lose its performance quality compared to the simulated data. Unfortunately, the other phase plate type did not live up to our expectations.

Table of Contents

Introduction

Conventional optical components are not capable of manipulating the phase and amplitude of incident light spatially. That is why diffractive optical elements (DOEs), such as beam shapers, beam splitters, pattern generators, gratings and kinoforms, have been developed that enable miscellaneous complex optical functions with accurate and constant properties to create outputs with unique functionalities[1–5]. Their ubiquity in optics make DOEs widely used in light and electron microscopy. Phase plates are a large subdivision of DOEs that are vital for research wherein phase-contrast microscopy is involved. For example, defocus can be omitted for the visualization of weak-phase objects when contrast enhancement is applied in Zernike phase-contrast light[6–8] and transmission electron microscopes[9–14]. Besides the DOEs used for the just mentioned imaging techniques, DOEs can conveniently engineer the point spread function (PSF) to encode extra physical properties[15–17]. Manufacturers offer high-quality glass etched phase plates that can be customized to the user's liking to alternate the size, shape, orientation, etc. of the PSF. However, the process of fabricating and delivering these phase plates is typically slow (at least a few working days) and expensive for low quantities. A more rapid, low-cost solution is to self-produce phase plates with a 3D printer, but imperfections in fine features that require µm precision originate easily, which will distort the wanted effect.

To evaluate the performance of any microscope set-up quantitatively, the PSF is acquired to visualize the degree of blurring. Normally, fluorescent microspheres – objects that represent infinite small point sources as closely as possible – are used as a calibration standard for this purpose and their PSF appears in the shape of a prolate spheroid with the major axis in the axial dimension. A phase plate pattern additionally modifies the PSF shape of the recorded object, but this only works when the DOE is placed at the Fourier plane. This could be accomplished by using the following approach: two identical positive lenses are placed in a mirrored position, whereby they create a new image plane. The phase plate is placed at the back focal plane (= Fourier plane) of the first lens (Fig. 1a), where the wavefront of the emitted light is aberrated, which is attributable to the height of the phase plate pattern delaying certain regions of the beam more than others. If all relay components and the camera are aligned perfectly, the pattern's quality is the determinative factor for the clarity of the introduced effect.

To reduce fabrication costs, phase plates can be 3D printed with two-photon polymerization (TPP), which relies on the simultaneous absorption of two photons in a transparent photosensitive material (photoresist). Monomeric resist undergoes polymerization by so-called photo-initiators that are activated and turned into radicals. Liquid non-polymerized photoresist is then washed out to uncover the solid cross-linked polymer structure. The superior resolution of TPP is based on the much lower probability of absorbing two photons at once than just one photon that carries enough energy in single-photon polymerization. Thus, cross-links are formed only in the area where the focus laser is deployed, because each photon in TPP carries half the energy required for polymerization, meaning that single photons are ineffective. At best, the finest 3D printed features reach a resolution of 100 nm with TPP[18–20]. Since phase plates commonly consist of a high refractive index (RI) material, there is a significant RI gap with air ($n \approx 1.000$). Due to its relation with the phase plate height, however, the major drawback is that this height should only be ± 1 µm to achieve an optimal phase shift. This means that flaws ≥ nm in the phase plate pattern are not tolerated during fabrication. Thus, realizing satisfactory phase plates is a fundamental challenge, especially when using a 3D printer that cannot fulfil the resolution target.

Recently, Orange-Kedem et al. demonstrated a method to simplify DOE fabrication by controllably scaling up the relevant feature dimensions of DOEs > 100 times. Phase masks were immersed in a medium that closely (but not perfectly) matches the RI of the 3D printed devices (Fig. 1d+e), and their height was redefined accordingly to preserve the same wavefront abberation[21]. They argued that the amount of phase shift can be managed by replacing the immersion liquid, praising the method's versatility. However, each phase masks takes about one working week to be produced, so if anybody wants to investigate a myriad of different patterns, just the fabrication alone would already be a labour-intensive assignment. Hence, we would like to elaborate on the idea of DOE immersion by including fabrication time as a factor.

Here, we demonstrate two types of high-quality phase plates, immersed in a solidified photoresist that had a slightly different RI than the photoresist used to print the phase plate with. Not only was the immersion process quicker, but the phase plate design was also more practical. Our choice of relay lenses to decrease the lateral phase plate size made it possible to fabricate one complete phase plate from scratch in just one day. After assembling and aligning the relay, the PSF was first evaluated in the absence of any phase plate to ensure a trustworthy baseline for comparisons. This evaluation was repeated after the implementation of the phase plates to characterize the alterations. The distorted PSF shapes were evident and one phase plate type was roughly in agreement with simulations

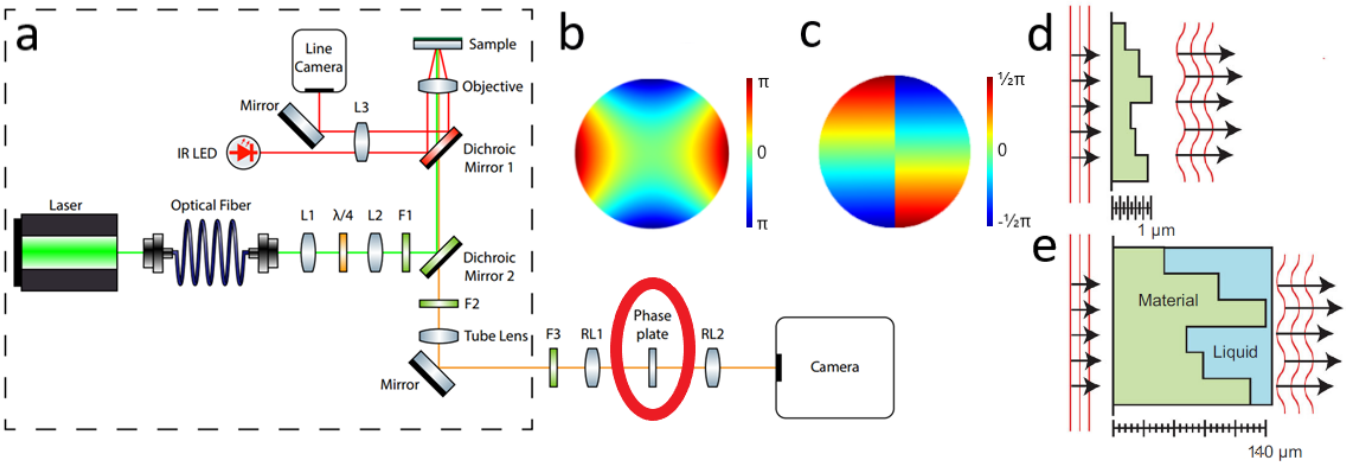

Figure 1 The concept of PSF engineering with immersed phase plates. (a) Schematic of our inverted light microscope with custom-built relay (comprehensive set-up description can be found in Materials & Methods). Lenses 1, 2 and 3 are abbreviated as L1, L2 and L3, the waveplate as λ/4, filters 1,2 and 3 as F1, F2 and F3, and relay lenses 1 and 2 as RL1 and RL2. Optical components cannot be inserted in the optical path within the dashed square. The saddle (b) and double vortex (c) phase plates are placed in the Fourier plane between the relay lenses (red ellipse), and their surface profiles induce the observed PSF distortion. (d-e) Schematic side view of the phase plates, whereby the pattern height without (d) and with (e) immersion substantially differ to introduce the same phase delay. Partially adapted from Hulleman *et al.*, 2021 (Nature Communications) and Orange-Kedem *et al.*, 2021 (Nature Communications).

that were carried out beforehand. Yet, the other phase plate operated unsatisfactorily, perhaps as a consequence of its more troublesome structure. This presumably resulted in a production flaw that could not be detected by visual examination.

Results

The phase plate surface profile regulates how much and where phase shift occurs at different regions of the emitted beam. The pattern quality is pivotal to adequately engineer the PSF, so we want to challenge the abilities of our 3D printer, because we expect that smoother surfaces are easier to construct than rough, uneven surfaces with many disruptions. Therefore, two substantially different types of phase plates were investigated: the astigmatic phase plate (Fig. 1b) that is continuous, shaped like a saddle (henceforth referred to as saddle phase plate) and introduces astigmatism, and the vortex phase plate (Fig. 1c) that contains discontinuities, shaped like an upward spiral and introduces primary spherical aberration. Their surface profiles can be represented as follows:

$$s(x) = a_s \cdot (x^2 - y^2) \quad (1)$$

$$v(x) = a_v \cdot \frac{c}{\pi} \cdot arctan\frac{y}{x} \quad (2)$$

where x and y express any given point on the length and width axes of the phase plates; a_s and a_v are the amplitudes of the saddle and vortex phase plate respectively; and c/π is a normalization constant. The value of c is equivalent to the number of spirals.

Systematically selecting the relay components to deduce the phase plate specifications

The amount of phase delay we want to introduce calls for a predetermined plan for phase plate fabrication. Considering this, the phase plates' amplitudes and material for their production are the foremost parameters to figure out (Fig. 2a). The astigmatism increases proportionally with the amplitude of the saddle phase plate, so any value could be selected, as long as the generated effect is significant. Contrastingly, the vortex phase plate's amplitude is much more stringent due to the discontinuous shape. In general, the accumulated phase difference experienced by the light that traverses through any phase plate can be described as:

$$\Delta\phi(x,y) = \frac{2\pi h(x,y)}{\lambda} \cdot (n_{DOE} - n_{media}) \quad (3)$$

where $\Delta\phi$ is the accumulated phase difference; h is the height of the phase plate profile; λ is the wavelength; and n_{DOE} and n_{media} are the RIs of the phase plate and the surrounding media respectively. Their difference will be referred to as Δn. The permitted fabrication error can be estimated by describing the accumulated phase error:

$$\delta\Delta\phi_{Error} = \Delta\phi_{Actual} - \Delta\phi_{Target} \quad (4)$$

$$= \frac{2\pi}{\lambda} \cdot (\Delta n + \delta n) \cdot (h + \delta h) - \frac{2\pi}{\lambda} \cdot \Delta n \cdot h$$

$$\xrightarrow{\delta n, \delta h \ll \Delta n, h} \frac{2\pi}{\lambda} \cdot \Delta n \cdot \delta h + \frac{2\pi}{\lambda} \cdot h \cdot \delta n$$

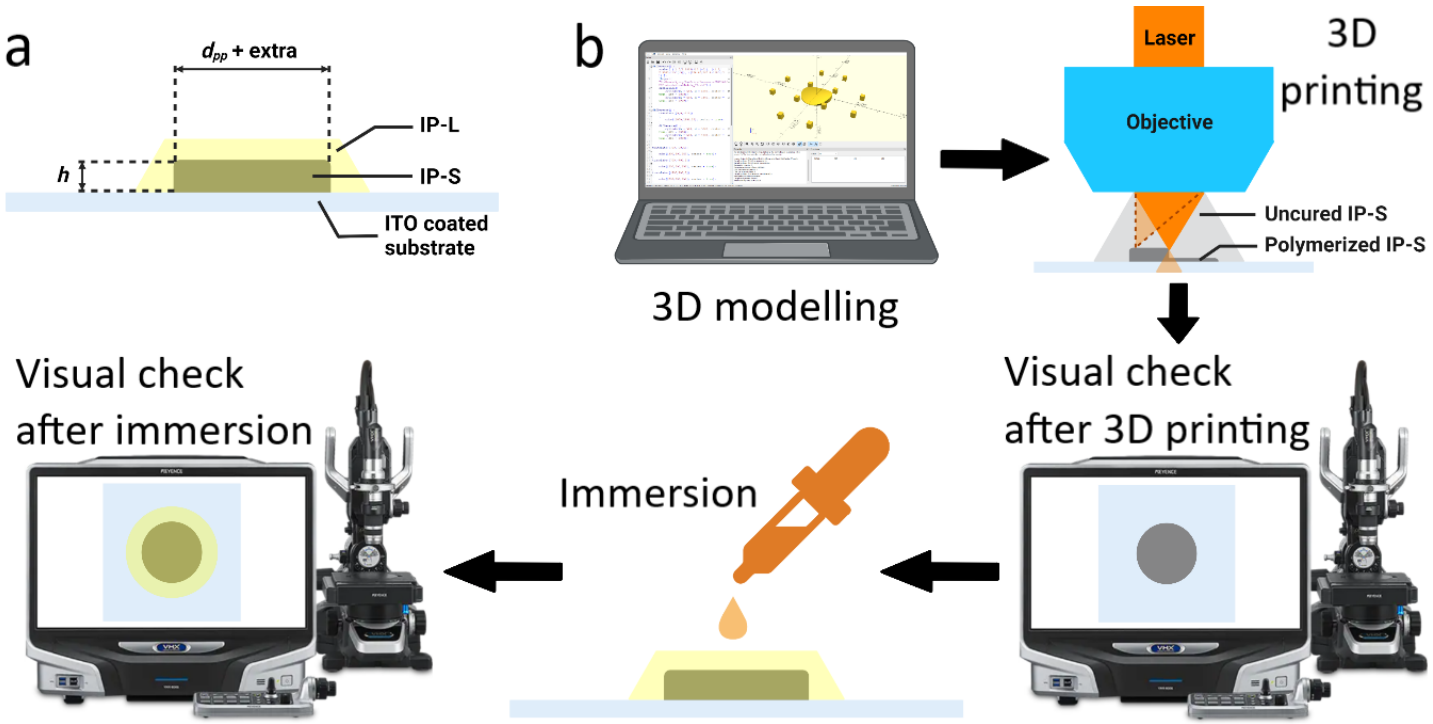

Figure 2 An overview of all steps taken to realize the phase plates. (a). A visual representation of all parameters that were considered before phase plate fabrication could commence. Apart from their surface profile, the only dissimilarity between the saddle and vortex phase plate was the phase plate height (h). The beam diameter at the phase plate position (d_{pp}) was broadened with 0.3 mm (= extra) to make phase plate alignment simpler later on. (b) The fabrication workflow comprised of three main steps: the 3D modelling, the 3D printing and the immersion of the phase plates. Two quality checks were implemented in between to intercept phase plates with defects.

where $\delta\Delta\phi_{Error}$ is the unwanted accumulated phase difference, deviating from the desired phase shift; δh is the height error from DOE fabrication; and δn is the error in RI difference between the DOE and the surrounding media. Most interestingly, Eq. (3) and Eq. (4) disclose that phase plates could be thicker with a more tolerable inaccuracy when Δn is smaller, but not zero. This improved tolerability is in our favour, since polymer structures fabricated with TPP can shrink[22], which is the main reason why height errors emerge. On the other hand, very small values for Δn increase the required height and thus the printing time of the phase plates greatly. In essence, we are faced with a trade-off between the tolerable height inaccuracy (better when Δn is smaller) and production duration (better when Δn is larger).

Out of several options for printing material, IP-S (n = 1.515) was chosen for phase plate fabrication, because it is ideal for mesoscale structures with a high proximity effect and has low shrinkage compared to other photoresists. The proximity effect refers to the variations in the linewidth of a feature as a function of the proximity of other nearby features. Large proximity effects in stereolithography are characterized by backscattered electrons that can travel many microns, thereby exposing photoresist at nearby features. Normally, when surrounded by air and λ = 560 nm, the phase plate h should be only slightly larger than one micron, but now that the phase plates will be immersed in photoresist IP-L (n = 1.519), their axial size and error tolerability are enlarged by almost 130 times owing to Δn = 0.004. The excitation laser was set at λ = 561 nm by reason of the phase plates' transmittance. IP-S and IP-L reflect or absorb light at various wavelengths, but the extinction coefficient of these photoresists are very low at 560 nm[23].

The desired phase delay is induced by the height of the phase plates, but also their length and width are important as the entire beam should fully hit a phase plate. The tube and relay lenses' strength of convergence controls the beam size at the back focal plane of the first relay lens, which is equal to the minimum requisite lateral size of the phase plates:

$$d_{pp} = d_{obj,tube} \cdot \frac{f_{RL}}{f_{tube}} \qquad (5)$$

where d_{pp} is the diameter of the beam when it passes through the phase plate; $d_{obj,tube}$ is the diameter of the beam in between the objective and tube lens; and f_{RL} and f_{tube} are the focal lengths of the relay lens and tube lens respectively. Two parameters are fixed due to the closed optical path of our microscope (Fig. 1a): $d_{obj,tube}$ = 6.0 mm and f_{tube} = 200 mm. Thus, our choice which lenses to utilize for relaying the original image plane determines the lateral size of the phase plates.

DeScribe, the software for preparing the printing job, implements a preview window wherein the printing time is predicted. We aim to develop a relatively rapid phase plate fabrication process, and therefore settled on a circular phase plate size with a diameter of 1.5 mm that takes approximately four to five hours to print if h = 140 µm (calculated from Eq. 3). The alignment of phase plates will be easier if the beam size is narrower than the phase plate diameter, so relay lenses with f_{RL} = 40 mm were chosen to make d_{pp} = 1.2 mm. The ray and wavefront aberrations by these lenses were insubstantial, as assured by ray behaviour simulations throughout the relay lenses compartment (Fig. S1). Now, we meet all requisites to produce and subsequently test phase plates.

The fabrication workflow: from outlined models to finalized apparatuses

In pursuit of the decisions made with regard to the variables, phase plate fabrication involving three major steps was executed according to our plan of action (Fig. 2b). First, the phase plates and surrounding pillars to hold a cover slip were modelled as 3D solid structures in OpenSCAD, a computer-aided design (CAD) program. PSF simulations – discussed in more detail later – unveiled that at h = 200 µm, sufficient astigmatism would be introduced by the saddle phase plate, so this value was selected based on profound judgement. More methodologically exact, the vortex phase plate height was calculated from Eq. 3. However, the spiral's apex exceeded the free working distance of the 3D printer's objective, so its realization was impossible this way. To make the printing feasible, while keeping the anticipated phase delay, two spirals with half the height of the initial single spiral were integrated in the vortex phase plate (h = 140 µm). The generated effect is indistinguishable, because each spiral in the double vortex was now portrayed as a two quadrant inverse tangent over interval $[-½\pi\,;\,+½\pi]$ with c = 2 instead of a four quadrant inverse tangent over interval $[-\pi;+\pi]$ with c = 1 in the single spiral case (see Eq. 2). An auxiliary benefit is that the structure of the double vortex phase plate embodies less volume, which reduces printing time. However, a second spiral also means a second discontinuity in the vortex phase plate, making it more arduous to print.

The second step was turning the 3D models into physical phase plates. Printing was done by polymerizing IP-S on glass substrates coated with indium tin oxide (ITO) on one side, making the glass highly transparent. The configuration used to write the structures, was dip-in laser lithography (DiLL). In this procedure, the objective lens is directly dipped into the liquid uncured photoresist, which acts as both a photosensitive and immersion medium. The 3D printer completed the manufacturing of one saddle (d = 1.5 mm; h = 200 µm) and one double vortex (d = 1.5 mm; h = 140 µm) phase plate somewhere between four to five hours per phase plate. After printing and uncured IP-S removal through incubation, the devices were inspected with a digital microscope to guarantee the absence of defects (Fig. S2). In addition, the instrument reconstructed the phase plates and estimated their heights, which were 175.04 µm for the saddle phase plate and 133.91 µm for the double vortex phase plate. This would correspond to a shrinkage rate of 12.48% and 4.35% respectively. We reckoned that these rates were respectable, even for the saddle phase plate. Induced astigmatism intensifies and weakens in a progressive manner, so a phase plate height of 175 µm instead of 200 µm will still clearly stamp its mark on the PSF.

Finally, IP-L was poured over the phase plates with care and entirely solidified. Between these actions, a cover slip was placed on top of the printed pillars to create a planar perpendicular surface of IP-L with regard to the emitted beam. Otherwise, the light will experience an uneven delay because of the irregular IP-S surface, and the PSF will not represent the pure phase plate effect. Examination with the digital microscope verified that no uncured photoresist was left, and that the phase plates were not damaged during the immersion process (Fig. S3). Furthermore, the view of the cover slips being parallel to the substrates was now better perceptible. If they are not parallel, refraction will steer the beam with an angle larger than zero towards the phase plate, second relay lens and image plane. Also, the phase plate will delay the beam unfavourably, all ultimately resulting in a deformed final image. In total, the post-processing steps took about two to three hours. In brief, the phase plates were produced in one working day per phase plate and complied with the visual criteria, so now their quality could be assessed. However, before proceeding with phase plate experiments, the PSFs without and with phase plates were simulated to raise expectations.

PSF simulations provide a good insight into the potential of the phase plates

Understanding image formation is crucial when we want to generate these artificially. The PSF is the impulse response function of an optical imaging system. The image is then the convolution of that object and the PSF. Our optimal situation would be an infinite small point source as object depicted by a diffraction-limited and aberration-free imaging system. However, the size of fluorescent microspheres is a real number (diameter = 175 nm), and perfect alignment of microscope components is near-impossible. With this

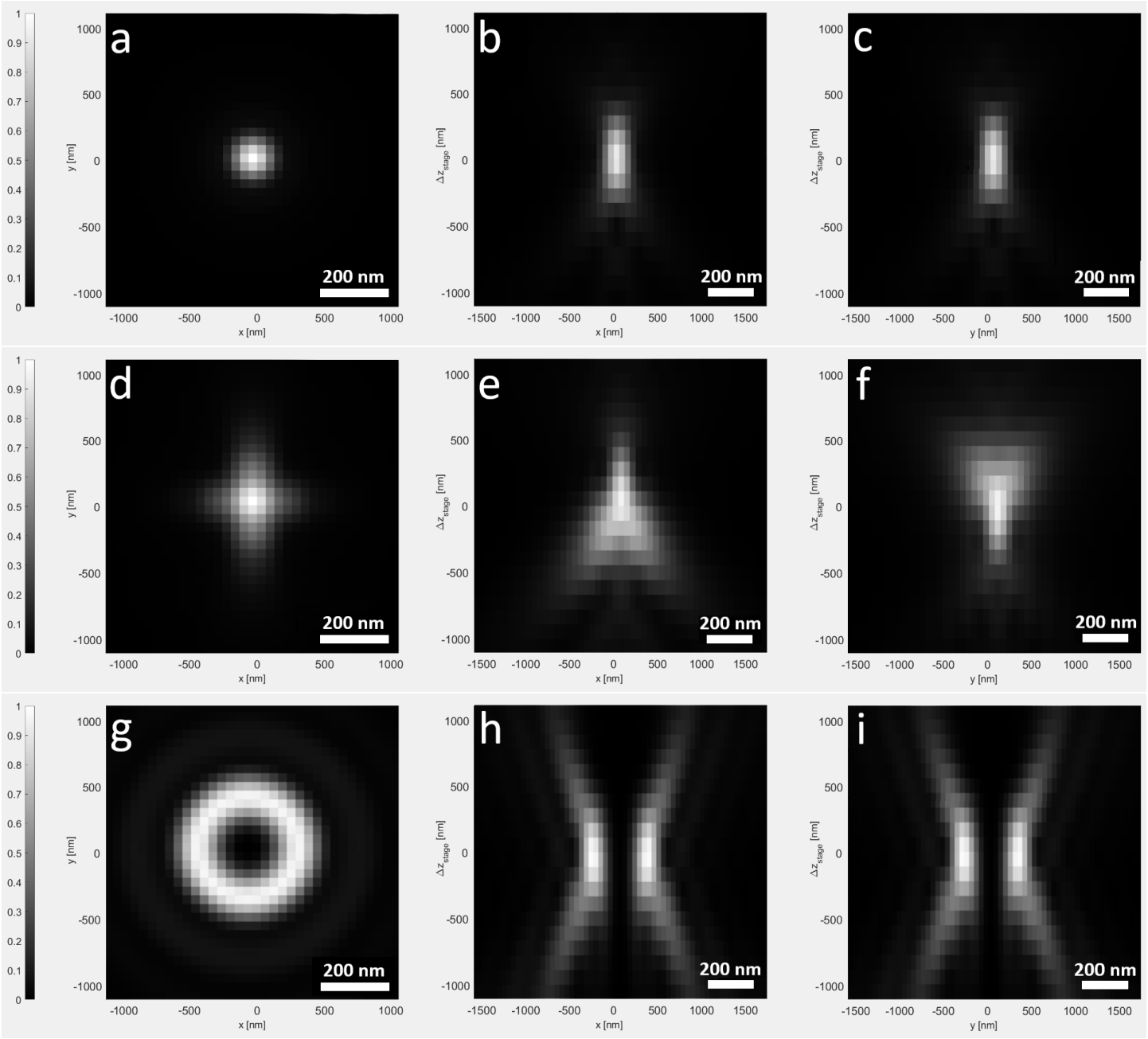

Figure 3 Simulated PSFs that change in shape and intensity with inclusion of the phase plate effect. The XY (a,d,g), XZ (b,e,h) and YZ (c,f,i) appearances of artificially generated PSFs are demonstrated without any phase plate (a-c), with the saddle phase plate (d-f) and with the double vortex phase plate (g-i). The saddle phase plate gives rise to a typical astigmatic effect on the microsphere, while a primary spherical aberration-like behaviour is perceived with the double vortex phase plate.

in mind, our simulation defined the object and the aberration function, which was split into the aberrations by misalignment and aberration introduced by the phase plate effect. It is feasible to realistically mimic the microspheres and the phase plate effect, but too much uncertainty is present when addressing the total aberration function. Hence, we went for a forward simulation that convoluted the microspheres with the total aberration function. Herein was assumed that no misalignment aberrations will be introduced by the microscope and relay components, and that phase plates (with ideal height) behaved perfectly.

The PSF for a microsphere emitter with fixed or free dipole axis was calculated using the chirp Z-transform (CZT) function with arbitrary windows and discretization in real and spatial frequency space. The original PSF of the emitter was a realistic portrayal of a microsphere in XY, but it was more elongated in the z-dimension (Fig. 3a-c). This PSF can be modified by adding a phase plate surface profile to the aberration function that partially defines the pupil matrix. With the saddle phase plate, unmistakable characteristics of astigmatism are discernible. The XY plane displays a cross shape, and the vertical and horizontal signals have different foci, which is best seen in the XZ and YZ planes (Fig. 3d-f). The double vortex phase plate

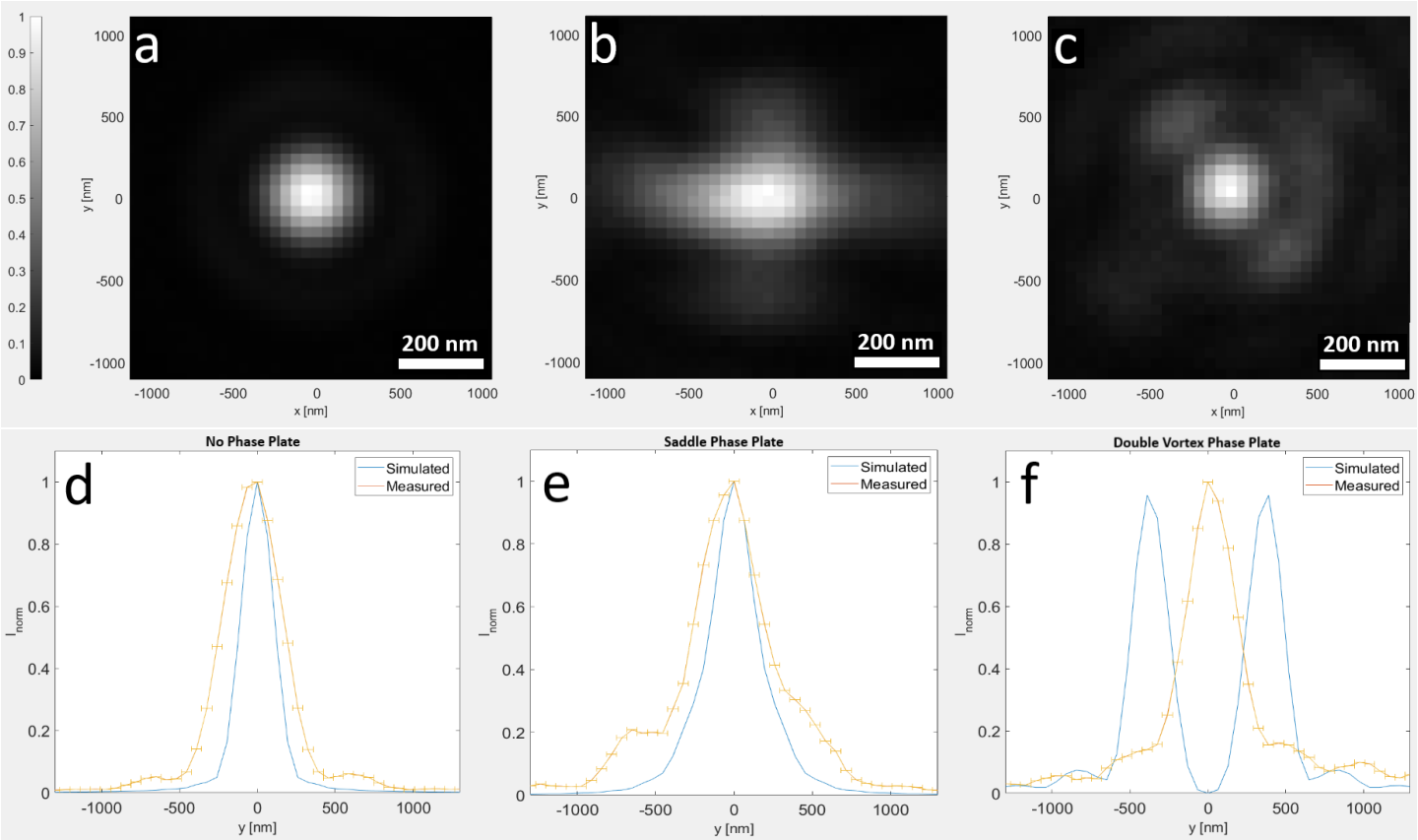

Figure 4 Experimentally obtained PSFs distorted by the 3D printed phase plates, and comparison with the artificially generated PSFs. The XY appearances of experimentally generated PSFs are demonstrated without any phase plate (a), with the saddle phase plate (b) and with the double vortex phase plate (c). The astigmatic effect by the saddle phase plate is undeniably recognizable. The double vortex phase plate induces only a very faint aberration and the PSF without phase plate is still largely present in these panels. The simulated and experimental data were compared quantitatively by plotting the intensity along the y-dimension (the (d) panel for the PSF without phase plate, the (e) panel for the PSF with the saddle phase plate, and the (f) panel for the PSF with the double vortex phase plate.

causes a donut-shaped signal with zero intensity in the centre, and the signal gets increasingly more out-of-focus when moved away from the focal plane (Fig. 3g-i). Although we are already aware that there will be a disparity with reality, the simulations confirm the phase plates' abilities and the effectiveness of our plan of action.

The fabricated phase plates distorted the PSF, but only the saddle phase plate did it as anticipated

The quality of the saddle and double vortex phase plates were methodically deduced through a side-by-side comparison with the artificial data. A meticulous alignment was carried out in advance to appreciate the pure phase plate effect as much as possible. The shape of the original PSF did not deviate much from its simulated lookalike (Fig. 4a), which is a validation that all components were aligned properly. The intensity spectrum along the y-dimension was used to quantify the artificial and experimental PSF sizes through measuring the full width at half maximum (FWHM) (Fig. 4d). Compared to the actual width of 175 nm, the microsphere came out merely broader in the simulation with 200 nm, whereas the measured PSF was 450 nm. Incorporating the saddle phase plate into the relay set-up induced the expected astigmatism, as the characteristic cross shape was clearly present (Fig. 4b). The intensity spectrum of the PSF was also equivalent to the artificial data (Fig. 4e). The vastness of both the simulated and measured microsphere enlarged, now being 320 nm and 500 nm respectively. With the double vortex phase plate in the relay lay-out, the PSF was unfortunately not aberrated much, as the original PSF was still predominantly extant (Fig. 4c). Typically, as displayed by the simulation's intensity spectrum, two peaks with a FWHM of 250 nm should arise with the double vortex phase plate is operated (Fig. 4f). However, the experimental PSF resembled more with the original PSF's measured data (Fig. 4d), showing a peak with a FWHM of 400 nm (Fig. 4f). The most perceptible distortion created was the weak signal directly encircling the original PSF (Fig. 4c). A couple of explanations why the double vortex phase plate performed so unsuccessfully are plausible. First, the discontinuities in the double vortex phase plate pattern are important for the height difference, but are

also the most delicate features of the device. They could have been too problematic for our 3D printer, which would induce a decrease of the height difference and ultimately would disturb the intended accumulated phase difference. In addition, the shrinkage of IP-S could have been too severe, even though the shrinkage rate of the double vortex phase plate was estimated to be < 5%. Another reason could be the wavelength of the emission beam. The wavelength of the excitation laser is 561 nm, but the microspheres emitted photons that were lower in energy, meaning that the wavelength of the emission beam was longer. Thus, an according increase of the phase plate height is necessary if the wavelength increases, which can be derived from Eq. 3. We computed that the spectrally weighted average for the wavelength would be 585 nm with an excitation wavelength of 561 nm, but we stuck to the emission maximum (560 nm) for safety.

The axial resolution was also inspected, taking into account that it is always worse than the lateral resolution of fluorescent microscopes. The lateral resolution is inversely proportional to the numerical aperture (NA) of the objective lens, whereas the axial resolution is inversely proportional to the squared NA. However, all spectral intensity plots showed that the signal in the z-dimension was stretched out too excessively to be true. These data are unacceptable as results and are therefore not shown. However, it also implies that it emerged independently from the effects induced by the phase plates. In summary, The PSF evaluation disclosed that the experimental outcomes without any phase plate and with the saddle phase plate closely approximated their artificial counterparts. The double vortex phase plate did not live up to our presumptions, probably due to anomalies that arose during fabrication. However, the fabrication of our high-quality saddle phase plate was just one working day and we reckon that this can be done for any DOE through 3D printing.

Discussion

In this work, we demonstrated that the time span to self-manufacture 3D printed DOEs can be diminished significantly, while maintaining the functionality and the quality. We used phase plates for this purpose, that were immersed to augment their dimensions. The defined phase plate specifications, our selection of relay components, the 3D printing with DiLL and our way to immerse the phase plates all contributed to the quickness of our fabrication process. Through running simulations in advance, we concluded that the saddle phase plate adjusted the PSF as expected, whereas the aberration on the PSF by the double vortex phase plate was scarcely distinguishable. A fabrication error, small enough to not be spotted during our inspections with the digital microscope, was presumably the source of this malfunctioning. From other publications, it was clear that the difference between the designed 3D model and the printed structure remains one of the biggest challenges in self-manufacturing DOEs[24–26]. Surface wrinkling, insufficient mechanical stability of structural features and (anisotropic) shrinkage are the most common reasons for fabrication errors. Several propositions to solve these issues have been explored and could be relevant for us. The phase plate height in the 3D model of the double vortex phase plate can be increased to compensate for the shrinkage[27]. The shrinkage rate could be determined by printing a range of thicker phase plates (1 or 2 µm increment for instance) and subsequently testing which one performs best. This would elucidate the required amount of enlargement. Another helpful adjustment to the 3D model would be the inclusion of so-called shrinkage guides that achieve a more uniform shrinkage[28]. Finally, for more mechanical stability, the laser exposure time could be extended to enhance the cross-linking density[29]. However, the emergence of air bubbles becomes a greater hazard by applying this procedure (Fig. S5). Thus, the delicacy of the discontinuities and the (anisotropic) shrinkage of IP-S are cumulative factors that probably caused the reduction of the accumulated phase difference, but various solutions exist to counteract these. We realize that the saddle phase plate is also subjected to these effects. However, the continuity of the pattern creates astigmatism in a progressive manner, so a shrunken phase plate would only induce a little less astigmatism than it normally would.

In addition to the double vortex phase plate, the emission beam also operated non-ideally during the experiments. In order to derive h from Eq. 3, λ = 560 nm was taken, because it was the emission maximum of the fluorescent microspheres. However, photons emitted by the microspheres have experienced Stokes shift, resulting in an emission beam with a longer wavelength. Hence, according to Eq. 3, the double vortex phase plate height should be increased accordingly to the longer wavelength, for acquiring the optimal 2π accumulated phase difference. Although the spectrally weighted average of the emission wavelength was determined to be 585 nm, we used the known emission maximum to calculate h = 140 mm, and aimed to print a double vortex phase plate with this height.

Lastly, the axial resolution was substantially less than expected. Microscopes frequently deploy high NA oil objective lenses to achieve high-resolution imaging. These lenses are designed and optimised to work with glass coverslips that are placed on top of biological samples. An immersion fluid is used to replace the air by a higher RI medium, and thus to

couple the sample onto the objective lens. Preferably, the sample and mounting medium should have a matching RI, but this rarely occurs, because most biological samples contain water or other solvents with RIs lower than the immersion oil. Ultrapure water (RI = 1.33) was the main constituent of our microsphere samples as well, while we used an immersion fluid with RI = 1.52. It has been reported previously that this RI mismatch between the sample and mounting medium deteriorates the axial resolution in microscopy due to the spherical aberration[30–32]. It results in a general PSF broadening, a scaling error induced by a focal shift as a consequence of the distortion along the z-axis, and a decrease in peak signal intensity of the PSF with increasing penetration depth. These effects on the PSF and images definitely could explain the shortcomings in our observed PSFs. One group performed aberration correction with adaptive optics in a confocal microscope set-up[33], but unfortunately these are not yet available on commercial microscopes.

Based on the saddle phase plate, we are convinced that DOEs can be self-manufactured through 3D printing without compromising on performance quality. The key condition is that a thorough performance inspection is indispensable, which could lead to optimizations in the DOE model. Since our proposed workflow is cheap and quick, redoing the fabrication of the optimized model would not be an impediment. Many different kinds of DOEs exist, making them broadly applicable for optical set-ups.

Materials & Methods

Relay lens alignment simulations

Zemax OpticStudio software, version 17.5 (Zemax, Kirkland, Washington, USA) was used as simulation program to study the behaviour of rays through and the aberrations introduced by lenses with a focal length of 40 mm. A straightforward model was created wherein two Thorlabs AC254-040-A-ML lenses (Thorlabs, Newton, New Jersey, USA) were positioned with two focal lengths in between (Fig. S1a). Their geometry and properties were retrieved from the built-in lens catalogue of Zemax OpticStudio. In addition, point sources that generated a cone of light were positioned at one focal length before the first lens, and at -6.5, -3, -1.5, 0, 1.5, 3 and 6.5 mm from its centre. An image plane was positioned at one focal length after the second lens. After ray tracing, the wavefront aberration, field curvature and f*tan(θ) distortion were calculated and plotted (Fig. S1b-d). The f*tan(θ) distortion refers to the displacement of the beam (which depends on the product of the effective focal length (f) and the tangent of the deflection angle θ).

PSF simulations

The effect on the PSF generated by the phase plates were calculated via a forward simulation in MATLAB, version R2022a (The MathWorks, Natick, Massachusetts, USA) that implemented the surface functions of the phase plates (see Code Availability). First, all parameters that affect the PSF were defined after which the pupil matrix, field matrix and PSF were computed consecutively. Wavefront aberrations (described by the Zernike coefficients and the RI mismatch between the medium surrounding the sample and the medium from the lens to the sample) were included to mimic the real situation as closely as possible. The phase plate effect could be added during the pupil matrix calculation step if desired. Moreover, the amplitude values of the saddle and double vortex phase plate for the 3D printing step were determined. For the saddle phase plate, a range of values (steps of 50 µm) was tested until significant PSF distortion was achieved, which was at 200 µm. The double vortex phase plate amplitude was calculated with Eq. 3 and the simulated PSF distortion confirmed this value (= 140 µm).

Preparation of job files for 3D printing

The surface functions of the saddle and double vortex profiles were converted to solid 3D models by using the MATLAB function *surf2solid()*[34]. The resulting 3D models were converted into STL format by using *stlwrite()*. These STL files were imported in OpenSCAD to effortlessly change the size of the saddle (d = 1.5 mm; h = 200 µm) and double vortex (d = 1.5 mm; h = 140 µm) phase plates. Sixteen surrounding pillars (200x200x250 µm in the saddle phase plate model, and 200x200x200 µm in the double vortex phase plate model) to support the cover slip that will be added after immersion, were also included (Fig. S4).

The modified STL files of the saddle and double vortex 3D models were saved and imported into the DeScribe software, version 2.7 (Nanoscribe, Karlsruhe, Germany). The default values for most parameters of the IP-S 25x ITO Solid (3D MF) recipe were chosen, including the slicing (distance between two adjacent layers) and hatching (distance between two adjacent lines within a plane). Only three parameters were adjusted: 1. The base slice count was set to 10, to embed more layers within the substrate. 2. The exposure was set to constant. 3. In rectangular splitting mode, the block size was set to 220x220x220 µm, because the phase plates with pillars exceeded the objective writing field. To prevent air bubble formation, the laser power and scan speed in the produced GWL job file were changed to be 70% and 70000 µm/s respectively, ascertained by a dose test (Fig. S5).

3D printing phase plates

Fabrication was executed by direct laser writing (DLW) using two-photon polymerization on a Nanoscribe Photonic Professional GT system (Nanoscribe, Karlsruhe, Germany). The 3D printer employs a pulsed femtosecond fibre laser source at a centre wavelength of 780 nm. The laser power ranges between 50 mW and 150 mW at a pulse length between 100 fs and 200 fs and at a repetition rate of 80 MHz. The laser beam was focused onto the sample with a Zeiss LCI Plan-Neofluar 25×/0.8 Imm Corr DIC M27 objective for water, silicone oil, glycerine, or oil immersion (Carl Zeiss, Oberkochen, Germany). The samples consisted of photosensitive material IP-S (Nanoscribe, Karlsruhe, Germany) on 17.5x17.5x0.7 mm glass, which were cut from their original size (30.0x30.0x0.7 mm) with a DISCO DAD3220 dicing saw (DISCO, Tokyo, Japan). The glass was coated with indium tin oxide (ITO) on one side. Prior to printing, the substrates were cleaned by rinsing with acetone and isopropanol, and subsequently blow-dried with air. Two circular phase plates were printed: one saddle (d = 1.5 mm; h = 200 µm) and one double vortex (d = 1.5 mm; h = 140 µm) and were then incubated in propylene glycol monomethyl ether acetate for 25 min, and in isopropanol for 5 min to remove uncross-linked IP-S.

The printed structures were examined with the Keyence VHX-6000 Digital Microscope with VH-ZST Dual Objective 20-2000x zoom (Keyence, Osaka, Japan), which also could reconstruct the phase plates in 3D to measure and verify if the printed height differences were (almost) matching the intended values (Fig. S2). The phase plates were immersed in IP-L (Nanoscribe, Karlsruhe, Germany), which has a Δn = 0.004 compared to IP-S, and a 15 mm Ø No. 1.5H cover glass (Marienfeld Superior, Lauda-Königshofen, Germany) was laid on top of the surrounding pillars. Next, the phase plates were put inside a transparent compact storage container. This container incorporated two opposing tubes: one connected to an argon gas tank to let argon gas flow inside, and one to let it flow outside the container. After replacing air with argon gas in the container with the phase plates inside, it was placed under a UV nail lamp for 5 minutes to solidify IP-L. The phase plates were examined with the digital microscope again to verify that the phase plates and pillars were still intact, that all IP-L appeared as a solid and that the round cover slip was parallel to the substrate.

Fluorescent microspheres preparation

PS-Speck™ Microscope Point Source microspheres (Invitrogen, Waltham, Massachusetts, USA) with diameter

of 0.175 +/- 0.005 µm (smaller than the ±188 nm resolution limit of our microscope set-up), and with excitation/emission wavelength of 540/560 nm (orange) were 1000x diluted with ultrapure water, sufficient to prevent the formation of large clumps of beads that would strongly cluster. Bead clump formation was further reduced by gently mixing the contents of the Eppendorf tube with diluted beads before pipetting. Samples were made by pipetting diluted beads on 76x26 mm Menzel-Gläser microscope slides (Thermo Fisher Scientific, Waltham, Massachusetts USA), followed by waiting until they were dried up, and covering them with 22x22 mm No. 1.5H cover glasses (Marienfeld Superior, Lauda-Königshofen, Germany). The microscope slides and cover slips were cleaned beforehand with Thorlabs Premium Optical Cleaning Tissues (Thorlabs, Newton, New Jersey, USA) moistened with 70% ethanol (v/v).

Microscope set-up

The inverted microscope Nikon Ti-E (Nikon, Tokyo, Japan) uses a Sapphire 561-150 CW excitation laser (Coherent, Santa Clara, California, USA), which is coupled into a fibre. The beam is collimated by the first lens towards a λ/4 waveplate to convert the linearly polarized laser to circular polarization. Then, the beam is focused by the second lens onto the back focal plane of a Nikon CFI Apochromat TIRF 100XC Oil (Nikon, Tokyo, Japan) objective with NA = 1.49. In between the two lenses, the excitation spectrum is filtered by a Chroma ZET405/488/561/640x filter (Chroma, Bellows Falls, Vermont, USA), and the excitation and emission path are split by a Chroma ZT405/488/561/640rpc dichroic mirror (Chroma, Bellows Falls, Vermont, USA). Only the 561 nm laser + filter + mirror combination was used. The emission spectrum is filtered by a Chroma ZET405/488/561/640m-TRF filter (Chroma, Bellows Falls, Vermont, USA) before being focused by the tube lens. The beam went through a Semrock FF01-609/57-25 filter (Semrock, Lake Forest, Illinois, USA) that was screwed on the exit of the microscope's optical path. The original image plane was relayed by two Thorlabs AC254-040-A-ML lenses (Thorlabs, Newton, New Jersey, USA) without additional magnification resulting in a 65 nm pixel size in object space. The 3D printed phase plates were positioned at the Fourier plane between the two relay lenses (Fig. S6). The emitted signal was detected by a Hamamatsu ORCA Ⅱ Digital CCD camera C11090-22B (Hamamatsu, Hamamatsu, Japan). All components were calibrated and aligned properly before imaging. Specifically, the relay lenses and phase plates were held in Thorlabs CXYZ1/M mounts (Thorlabs, Newton, New Jersey, USA) which can translate in all three dimensions. This facilitated the fine re-alignment after phase plate substitution. The mounts with relay lenses were first solely aligned to each other via a general beam alignment procedure[35], before their alignment within the microscope set-up.

Imaging protocol

The Z-stack acquisition of the microscope is controlled with the NIS-elements software (Nikon, Tokyo, Japan), whereas the CCD camera uses its own HCImage Live software (Hamamatsu, Hamamatsu, Japan) to record images. Therefore, the camera was externally triggered by the stage movement of the microscope. Z-stacks with 201 frames, a 0.1 µm step size, 900 ms exposure and 10 mW intensity were made with and without the saddle or double vortex phase plate in a short period of time.

Data analysis

Z-stack data files were imported in ImageJ with Fiji as its distribution[36,37]. Across all Z-stacks, a rough cropping in xy-dimensions was performed around the visually best-looking beads that were isolated from others. For each bead, the pixel with highest intensity was identified with the FindFoci option of the GDSC plugin[38], and with further cropping, the beads were then centered around their respective highest intensity pixel. Thus, each pixel was positioned at x = 129 pixels, y = 129 pixels and z = 51st frame in a Z-stack of a single bead with 257x257 pixels in x and y and 101 frames. These individual bead stacks were then normalized in MATLAB and loaded into the script that plotted the simulated PSFs and intensities along the y- and z-dimensions, to make the same figures for the experimental data.

Code Availability

MATLAB code for PSF simulations is available on https://github.com/KJurgensTUD/PhasePlate_project_KJ.

References

1. Stankevičius E, Gecys P, Gedvilas M, et al. Laser Processing by Using Diffractive Optical Laser Beam Shaping Technique. *J Laser Micro/Nanoengineering*. 2011;6. DOI:10.2961/jlmn.2011.01.0009

2. Barlev O, Golub MA. Multifunctional binary diffractive optical elements for structured light projectors. *Opt Express*. 2018;26(16):21092-21107. DOI:10.1364/OE.26.021092

3. Siemion A. The Magic of Optics—An Overview of Recent Advanced Terahertz Diffractive Optical Elements. *Sensors*. 2021;21(1). DOI:10.3390/s21010100

4. Barré N, Jesacher A. Beam shaping of highly multimode sources with cascaded diffractive optical elements. *Procedia CIRP*. 2022;111:566-570. DOI:10.1016/j.procir.2022.08.151

5. Le Z, Liu Z, Qiu Y, Ren H, Dai Y. Fabrication of ultrathin flexible diffractive optical elements (DOEs) and application for laser speckle suppression. *Opt Lasers Eng*. 2022;159:107223. DOI:10.1016/j.optlaseng.2022.107223

6. Zernike F. Phase contrast, a new method for the microscopic observation of transparent objects. *Physica*. 1942;9(7):686-698. DOI:10.1016/S0031-8914(42)80035-X

7. Allen RD, Allen NS, Travis JL. Video-enhanced contrast, differential interference contrast (AVEC-DIC) microscopy: A new method capable of analyzing microtubule-related motility in the reticulopodial network of allogromia laticollaris. *Cell Motil*. 1981;1(3):291-302. DOI:10.1002/cm.970010303

8. Mehta SB, Sheppard CJR. Partially coherent image formation in differential interference contrast (DIC) microscope. *Opt Express*. 2008;16(24):19462-19479. DOI:10.1364/OE.16.019462

9. Danev R, Nagayama K. Transmission electron microscopy with Zernike phase plate. *Ultramicroscopy*. 2001;88(4):243-252. DOI:10.1016/S0304-3991(01)00088-2

10. Murata K, Liu X, Danev R, et al. Zernike Phase Contrast Cryo-Electron Microscopy and Tomography for Structure Determination at Nanometer and Subnanometer Resolutions. *Structure*. 2010;18(8):903-912. DOI:10.1016/j.str.2010.06.006

11. Schultheiss K, Zach J, Gamm B, et al. New Electrostatic Phase Plate for Phase-Contrast Transmission Electron Microscopy and Its Application for Wave-Function Reconstruction. *Microsc Microanal*. 2010;16(6):785-794. DOI: 10.1017/S1431927610093803

12. Tavabi AH, Beleggia M, Migunov V, et al. Tunable Ampere phase plate for low dose imaging of biomolecular complexes. *Sci Rep*. 2018;8(1):5592. DOI:10.1038/s41598-018-23100-3

13. Majorovits E, Barton B, Schultheiß K, Pérez-Willard F, Gerthsen D, Schröder RR. Optimizing phase contrast in transmission electron microscopy with an electrostatic (Boersch) phase plate. *Ultramicroscopy*. 2007;107(2):213-226. DOI:10.1016/j.ultramic.2006.07.006

14. Schwartz O, Axelrod JJ, Campbell SL, Turnbaugh C, Glaeser RM, Müller H. Laser phase plate for transmission electron microscopy. *Nat Methods*. 2019;16(10):1016-1020. DOI:10.1038/s41592-019-0552-2

15. Pavani SRP, Thompson MA, Biteen JS, et al. Three-dimensional, single-molecule fluorescence imaging beyond the diffraction limit by using a double-helix point spread function. *Proc Natl Acad Sci*. 2009;106(9):2995-2999. DOI:10.1073/pnas.0900245106

16. Shechtman Y, Sahl SJ, Backer AS, Moerner WE. Optimal Point Spread Function Design for 3D Imaging. *Phys Rev Lett*. 2014;113(13):133902. DOI:10.1103/PhysRevLett.113.133902

17. Shechtman Y, Weiss LE, Backer AS, Lee MY, Moerner WE. Multicolour localization microscopy by point-spread-function engineering. *Nat Photonics*. 2016;10(9):590-594. DOI:10.1038/nphoton.2016.137

18. Kawata S, Sun H-B, Tanaka T, Takada K. Finer features for functional microdevices. *Nature*. 2001;412(6848):697-698. DOI:10.1038/35089130

19. Sugioka K, Cheng Y. Ultrafast lasers—reliable tools for advanced materials processing. *Light Sci Appl*. 2014;3(4):e149-e149. DOI:10.1038/lsa.2014.30

20. Jiang LJ, Campbell JH, Lu YF, Bernat T, Petta N. Direct Writing Target Structures by Two-Photon Polymerization. *Fusion Sci Technol*. 2016;70(2):295-309. DOI:10.13182/FST15-222

21. Orange-Kedem R, Nehme E, Weiss LE, et al. 3D printable diffractive optical elements by liquid immersion. *Nat Commun*. 2021;12(1):1-6. DOI:10.1038/s41467-021-23279-6

22. Purtov J, Verch A, Rogin P, Hensel R. Improved development procedure to enhance the stability of microstructures created by two-photon polymerization. *Microelectron Eng*. 2018;194:45-50. DOI:10.1016/j.mee.2018.03.009

23. Schmid M, Ludescher D, Giessen H. Optical properties of photoresists for femtosecond 3D printing: refractive index, extinction, luminescence-dose dependence, aging, heat treatment and comparison between 1-photon and 2-photon exposure. *Opt Mater Express*. 2019;9(12):4564-4577. DOI:10.1364/OME.9.004564

24. Roca-Cusachs P, Rico F, Martínez E, Toset J, Farré R, Navajas D. Stability of Microfabricated High Aspect Ratio Structures in Poly(dimethylsiloxane). *Langmuir*. 2005;21(12):5542-5548. DOI:10.1021/la046931w

25. Takada K, Kaneko K, Li Y-D, Kawata S, Chen Q-D, Sun H-B. Temperature effects on pinpoint photopolymerization and polymerized micronanostructures. *Appl Phys Lett*. 2008;92(4):41902. DOI:10.1063/1.2834365

26. LaFratta CN, Baldacchini T. Two-Photon Polymerization Metrology: Characterization Methods of Mechanisms and Microstructures. *Micromachines*. 2017;8(4). DOI:10.3390/mi8040101

27. Sun H-B, Suwa T, Takada K, et al. Shape precompensation in two-photon laser nanowriting of photonic lattices. *Appl Phys Lett*. 2004;85(17):3708-3710. DOI:10.1063/1.1807019

28. Lim TW, Son Y, Yang D-Y, et al. Net Shape Manufacturing of Three-Dimensional SiCN Ceramic Microstructures Using an Isotropic Shrinkage Method by Introducing Shrinkage Guiders. *Int J Appl Ceram Technol*. 2008;5(3):258-264. DOI:10.1111/j.1744-7402.2008.02234.x

29. Park S-H, Kim KH, Lim TW, Yang D-Y, Lee K-S. Investigation of three-dimensional pattern collapse owing to surface tension using an imperfection finite element model. *Microelectron Eng*. 2008;85(2):432-439. DOI:10.1016/j.mee.2007.08.003

30. Hell S, Reiner G, Cremer C, Stelzer EHK. Aberrations in confocal fluorescence microscopy induced by mismatches in refractive index. *J Microsc*. 1993;169(3):391-405. DOI:10.1111/j.1365-2818.1993.tb03315.x

31. Diaspro A, Federici F, Robello M. Influence of refractive-index mismatch in high-resolution three-dimensional confocal microscopy. *Appl Opt*. 2002;41(4):685-690. DOI:10.1364/AO.41.000685

32. Egner A, Hell SW. Aberrations in Confocal and Multi-Photon Fluorescence Microscopy Induced by Refractive Index Mismatch BT - Handbook Of Biological Confocal Microscopy. In: Pawley JB, ed. Springer US; 2006:404-413. DOI:10.1007/978-0-387-45524-2_20

33. Booth MJ, Neil MAA, Juškaitis R, Wilson T. Adaptive aberration correction in a confocal microscope. *Proc Natl Acad Sci*. 2002;99(9):5788-5792. DOI:10.1073/pnas.082544799

34. Holcombe S. surf2solid - Make a solid volume from a surface for 3D printing. *MATLAB Cent File Exch*. Published online 2022. https://www.mathworks.com/matlabcentral/fileexchange/42876-surf2solid-make-a-solid-volume-from-a-surface-for-3d-printing

35. Wang J, Allgeyer ES, Sirinakis G, et al. Implementation of a 4Pi-SMS super-resolution microscope. *Nat Protoc*. 2021;16(2):677-727. DOI:10.1038/s41596-020-00428-7

36. Schindelin J, Arganda-Carreras I, Frise E, et al. Fiji: an open-source platform for biological-image analysis. *Nat Methods*. 2012;9(7):676-682. DOI:10.1038/nmeth.2019

37. Rueden CT, Schindelin J, Hiner MC, et al. ImageJ2: ImageJ for the next generation of scientific image data. *BMC Bioinformatics*. 2017;18(1):529. DOI:10.1186/s12859-017-1934-z

38. Herbert AD, Carr AM, Hoffmann E. FindFoci: A Focus Detection Algorithm with Automated Parameter Training That Closely Matches Human Assignments, Reduces Human Inconsistencies and Increases Speed of Analysis. *PLoS One*. 2014;9(12):e114749. DOI:10.1371/journal.pone.0114749

Supplementary Information

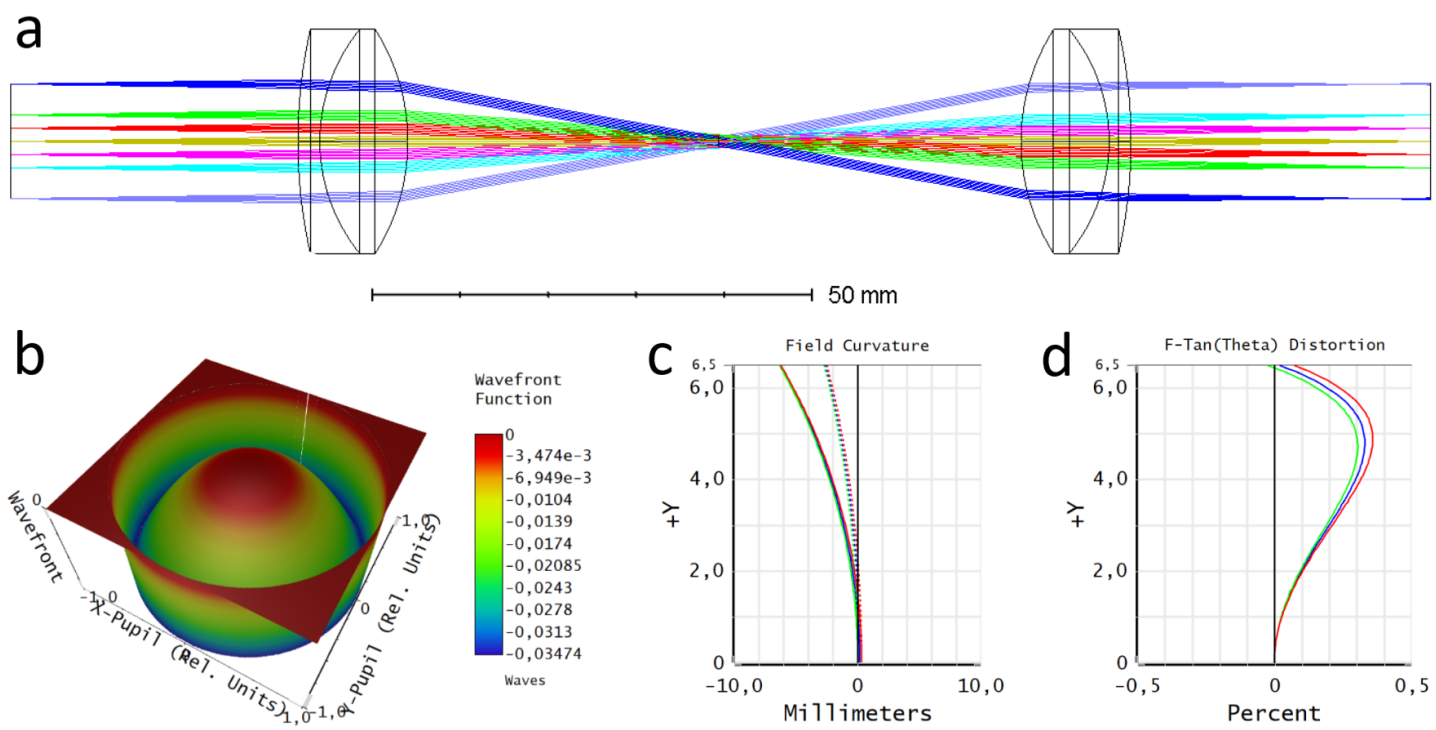

Figure S1 Optical behaviour simulations of relay lenses. (a) Illustration of two Thorlabs AC254-040-A-ML lenses, the original and newly created image plane, and point sources initiating from the original image plane at 0 mm (gold), 1.5 mm (red and dark pink), 3.0 mm (green and light blue) and 6.5 mm (dark blue and violet blue) from the center. All rays focus at the Fourier plane, and confirmed was that the beam size was 1.2 mm. (b) The wavefront aberration of a beam with λ = 560 nm, introduced by the relay lenses, is estimated by plotting an error map and calculating the root mean square (RMS) error (= 0.0100 waves). The RMS value expresses statistical deviation from the perfect reference spherical wavefront, averaged over the entire wavefront. (c) Plot of the field curvature in the XZ (dotted line) and YZ (solid line) planes of the beam for three wavelengths: 488 nm (green), 560 nm (blue) and 641 (red). (d) Plot of the f*tan(θ) distortion (the displacement of the beam) for the same wavelengths as in panel (c).

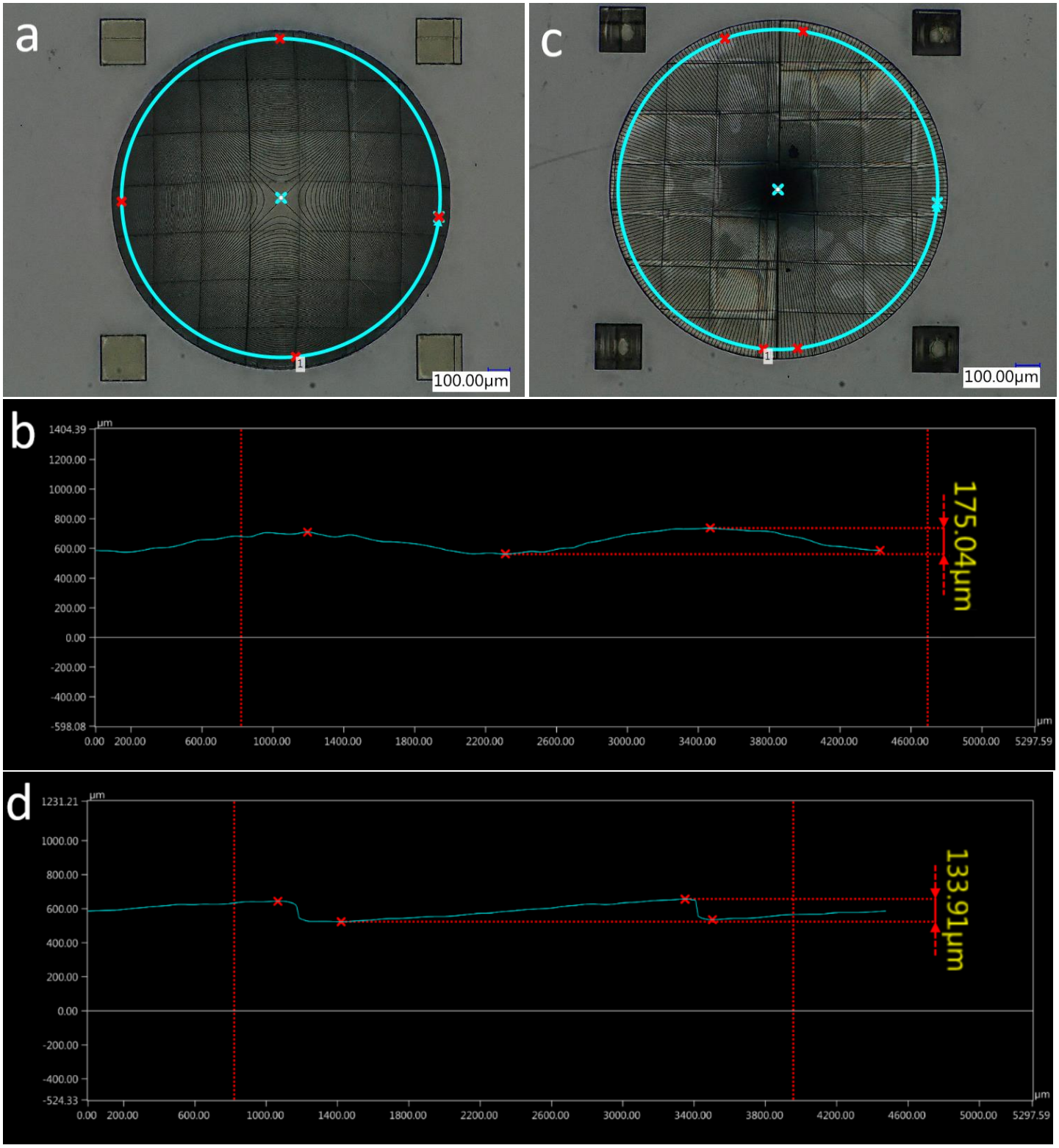

Figure S2 Phase plate height estimation. The digital microscope can reconstruct objects and implements miscellaneous tools to measure distances and determine highest / lowest values. Here, the phase plates were reconstructed in 3D by recording a Z stack and were displayed in (a) and (c) as 2D cross sections wherein the phase plates were automatically brought in focus by the microscope. In these cross sections, a round circle was drawn close to the edges of the phase plates (light blue), where the highest and lowest points on the phase plate are (indicated with red crosses). The yellow height values in (b) and (d) of the saddle (a-b) and double vortex (c-d) phase plate were found by subtracting the lowest minimum from highest maximum.

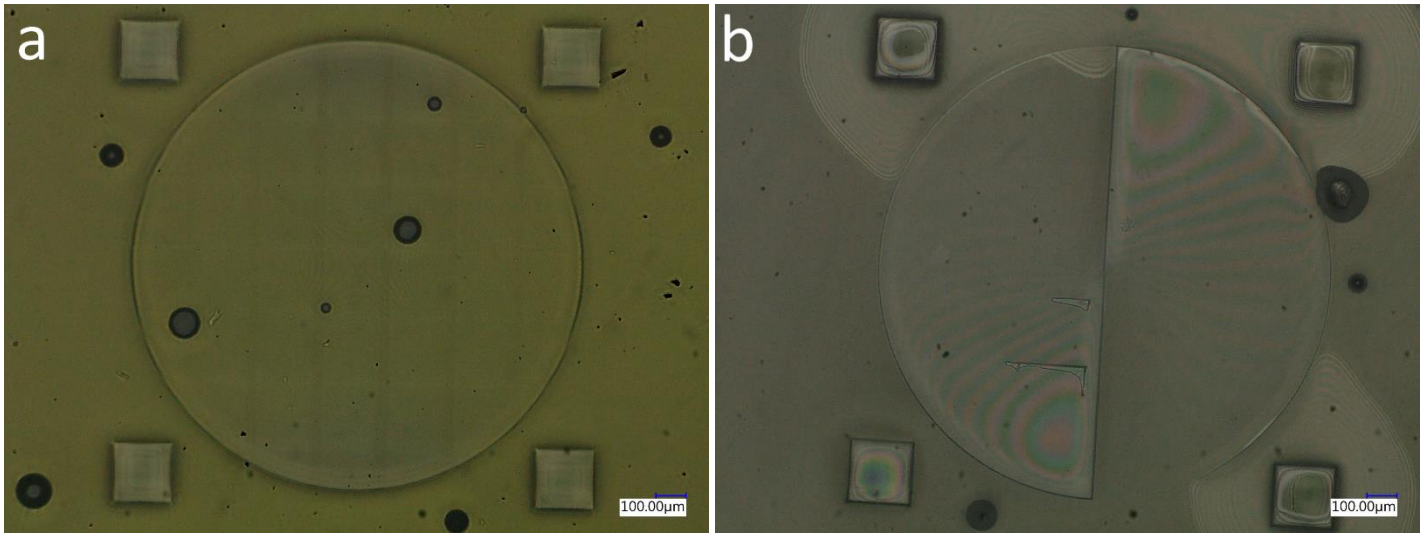

Figure S3 Checking the phase plates after the immersion process. These screenshots taken with the digital microscope display a consistent immersion of IP-L, covering the entire intact saddle (a) and double vortex (b) phase plates. The black stains are air bubbles, which could perturb the emission beam's trajectory if their presence is large-scale.

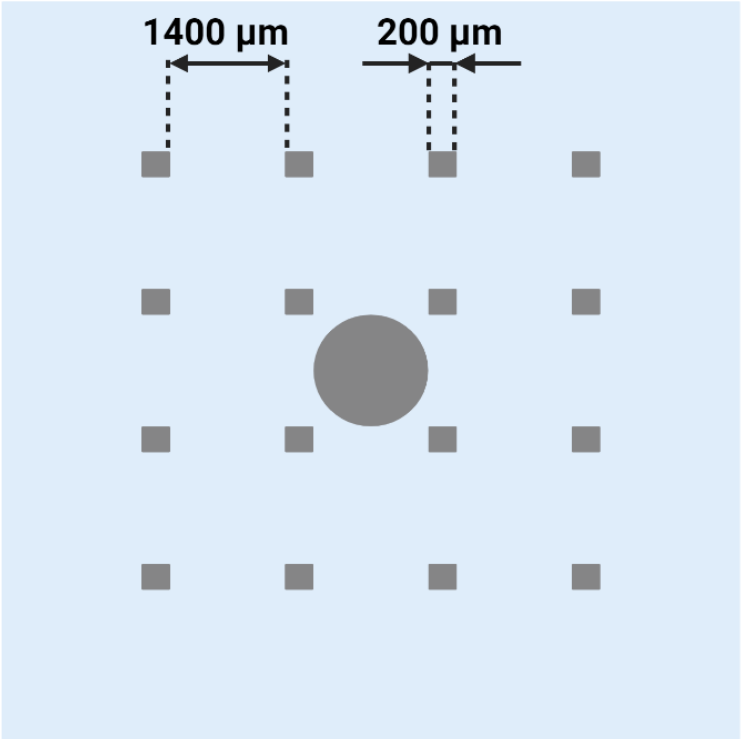

Figure S4 Supporting pillars around the phase plate to carry the round cover slip. Sixteen pillars formed a grid and the distance between two neighbouring squares was 1400 µm. Their length and width were 200 µm; the height was 200 µm for the saddle phase plate and 250 µm for the double vortex phase plate.

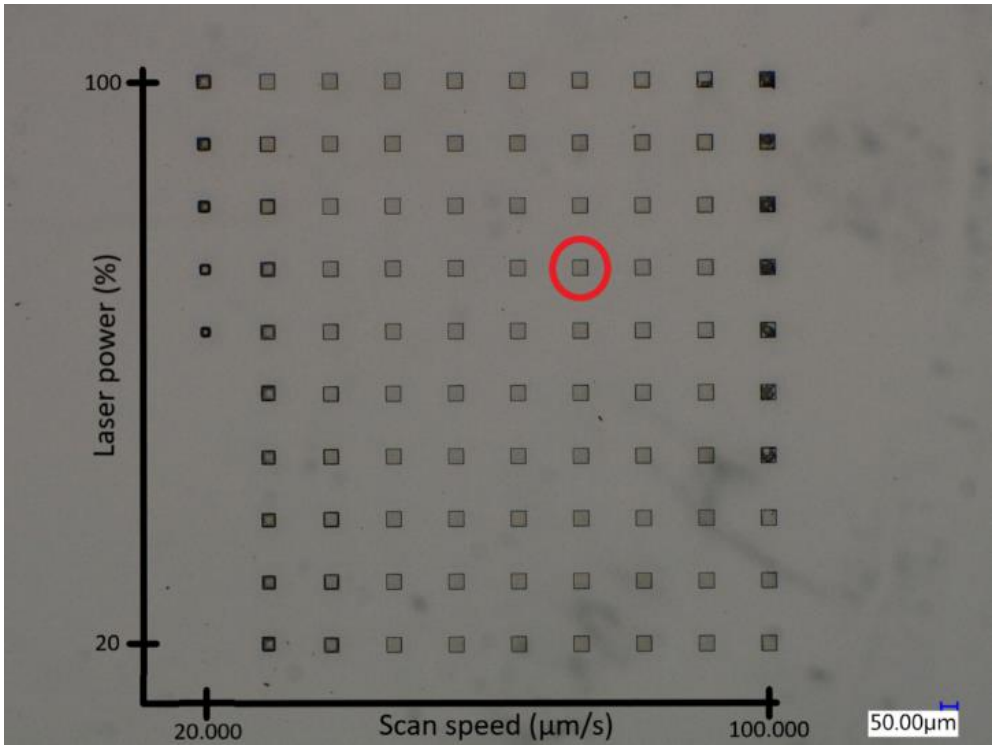

Figure S5 Dose test. Small cubes consisting of IP-S were 3D printed on a ITO coated glass substrate. The laser power varied from 20% to 100%, with steps of 10%. The scan speed varied from 20.000 to 100.000 µm/s, with steps of 10.000 µm/s. A combination of 70% and 70.000 µm/s (red circle) was a safe decision for printing quick while avoiding printing too intensely. Printing with too little or too much intensity promotes air bubble formation (black spots).

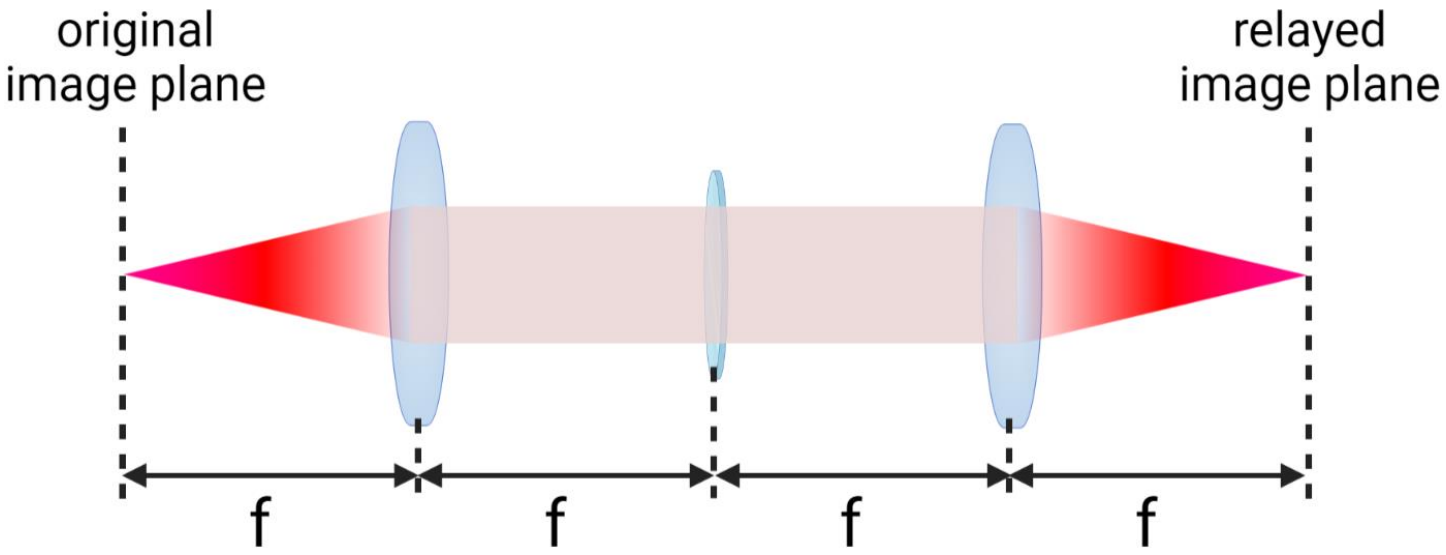

Figure S6 Cartoon representation of the relay path. Two Thorlabs AC254-040-A-ML lenses created a new image plane at exactly four times the focal length of these lenses (4f = 160 mm) from the original image plane. The beam diameter remained a constant 1.2 mm between the two lenses. The Fourier plane wherein the phase plates with 1.5 mm diameter were placed, was the back focal plane of the left relay lens.

-